Large regional variability in coastal erosion caused by ENSO

Kilian Vos (k.vos@unsw.edu.au)
Water Research Laboratory, School of Civil and Environmental Engineering, UNSW Sydney, NSW
https://orcid.org/0000-0002-9518-1582

Mitchell Harley
UNSW Australia https://orcid.org/0000-0002-1329-7945

Ian Turner
UNSW Australia https://orcid.org/0000-0001-9884-6917

Kristen Splinter
UNSW Australia https://orcid.org/0000-0002-0082-8444

Article

Keywords: Interannual Climate Variability, Oceanographic Forcing, Basin-scale Changes, Landsat Imagery

Posted Date: July 12th, 2021

DOI: https://doi.org/10.21203/rs.3.rs-666160/v1

Version of Record: A version of this preprint was published at Nature Geoscience on February 9th, 2023.
See the published version at https://doi.org/10.1038/s41561-022-01117-8.

Abstract

In the Pacific Basin, El Niño/Southern Oscillation (ENSO) is the dominant mode of interannual climate variability and drives substantial changes in oceanographic forcing, likely having a significant impact on Pacific coastlines. Yet, how sandy coasts respond to these basin-scale changes has to date been limited to a few long-term beach monitoring sites, predominantly on developed coasts. Here we use 35 years of Landsat imagery to map shoreline variability around the Pacific Rim (72,000 beach transects) and identify coherent patterns of beach erosion and accretion controlled by ENSO. We find that approximately one third of all beaches experience significant erosion during El Niño phases, with the Eastern Pacific particularly vulnerable to widespread erosion (most notably during the large 1997/1998 event). In contrast, La Niña events coincide with significant accretion for approximately one quarter of all beaches, although conversely drives substantial erosion in south-east Australia and other localized regions. The significant regional variability in coastal response to ENSO should be considered in light of future projected intensification and shifts in ENSO amplitudes and flavors.

Main Text

Sandy coasts comprise 31% of coastal environments worldwide[1], of which the majority are classified wave-dominated[2]. These coasts are particularly vulnerable to fluctuations in ocean wave energy and water levels, that drive cycles of erosion and accretion at episodic, interannual and decadal timescales, impacting adjacent infrastructure and beach habitats. The interannual timescale is of particular interest as it is closely linked to the Earth's climate and its internal modes of climate variability. In a changing climate, a likely intensification of these important climate patterns[3,4], coupled with projected changes in storminess[5,6] and rising sea levels, will likely exacerbate coastal erosion[7] and threaten the future resilience of many coastal communities worldwide[8,9].

In the Pacific Basin, El Niño/Southern Oscillation (ENSO) is the dominant mode of interannual climate variability and has teleconnections with a broad range of atmospheric and oceanic processes along coastal regions[10], influencing nearshore wave climates[11], sea-level anomalies[12] and river discharge[13]. Yet, our understanding of how sandy coasts in the Pacific respond to these basin-scale changes has to date been limited to a small number of long-term beach monitoring sites, predominantly located along developed coasts in North America, Australia and Japan[14–22]. Recent innovations in cloud data platforms[23] and remote sensing algorithms[24–26] have opened up the possibility for coastal change to be quantified at unprecedented global scales using satellite imagery. While this approach has been successfully used to identify global long-term trends in shoreline change over several decades[1,27], a major factor that has to-date limited the temporal resolution of satellite-derived coastal observations (including interannual variability) has been the effect of high-frequency tidal fluctuations, requiring the use of satellite composite images averaged over large temporal windows (i.e., annually). However, novel methods for beach slope estimation and tidal correction at the global scale[28] now make it possible to

map shoreline changes using individual satellite images (typically every 15 days for Landsat), significantly increasing the frequency of satellite-derived coastal data.

Here, we use individual satellite images to derive shoreline time-series spanning three Landsat missions (1984-2020) along wave-dominated sandy coastlines around the Pacific Basin. We present a detailed overview of the teleconnections between regional patterns of coastal erosion and accretion in the Pacific and ENSO. To further investigate the mechanisms responsible for the observed regional patterns of shoreline variability, we perform a basin-scale analysis of the variations in coastal wave energy flux and sea-level anomalies during the two opposite phases of ENSO. Lastly, we identify temporal patterns of extreme beach erosion associated with major ENSO events over the past 35 years.

Regional patterns of shoreline response to ENSO in the Pacific

Wave-dominated sandy beaches across the Pacific were identified and mapped based on the availability of Landsat images and use of the Relative Tidal Range (RTR = Spring Tidal Range/Average Wave Height) to distinguish wave-dominated (RTR<3) from more tide-dominated coasts (Methods, illustrated in Supplementary Figs. 1 and 2). The *CoastSat* toolbox[29] was then used to automatically map the shoreline position on Landsat 5 (1984-2013), Landsat 7 (1999-current) and Landsat 8 (2013-current) images. The resulting time-series of shoreline change were tidally-corrected using a global tide model and a satellite-derived estimate of the average beach slope[28], amounting to 72,000 beach transects in total across the Pacific.

To investigate the effect of ENSO on interannual shoreline variability, we evaluated anomalies in seasonally-averaged shoreline position during El Niño and La Niña phases at each transect. The Multivariate ENSO Index (MEI), considered as one of the most complete indices describing ENSO[30], was used to identify El Niño and La Niña periods during the past 35 years (Methods). We performed a statistical test (non-parametric Wilcoxon signed rank test) to assess whether shoreline anomalies during each phase were significantly different (at the 95% confidence level) to the long-term average. Also, with strong seasonal shoreline variability evident particularly in the northern hemisphere, where energetic wave conditions primarily occur during the boreal winter (DJF)[31], the anomaly analyses were carried out for both boreal winter shorelines as well as for all four seasons (see Methods and Supplementary Figs. 3 and 4).

Figure 1 summarizes the regional sandy coastline response to El Niño and La Niña phases for both the boreal winter-only analysis as well as all four seasons. Considering the entire Pacific, 69% of all transects indicate beach erosion during El Niño phases, of which 33% are statistically significant in both analyses (i.e., boreal winter and all seasons). Focusing on the regional variability, the Eastern Pacific (USA, Mexico, Peru and Chile) in particular is identified as showing a particularly coherent erosion response to El Niño phases, with 50% of transects (boreal winter) showing significant erosion (Fig. 1a). Concurrently, broad accretion is observed during El Niño phases along sandy beaches in south-east Australia, where more than 70% of transects (all seasons) experience significant beach accretion (Fig. 1c).

By contrast, during La Niña phases, 60% of all transects indicate beach accretion, of which 26% (boreal winter) and 24% (all seasons) are statistically significant. Positive shoreline anomalies are predominantly found in the Eastern Pacific, while widespread erosion is observed during La Niña phases along south-east Australia (45% of transects experiencing significant erosion for all seasons, Fig. 1d). Along the coasts of smaller island nations where suitable Landsat imagery were available (New Zealand, Japan and Hawaii), the shoreline data shows a mixed response to ENSO. While the proportion of statistically significant anomalies is not sufficient to infer a coherent regional response at these islands, it can be observed that Hawaii tends to erode during El Niño and accrete during La Niña phases (all seasons), as does Japan.

Changes in oceanographic forcing associated with ENSO

As sandy beaches generally erode in response to energetic waves and/or elevated water levels[7,32,33] and accrete during calmer periods[34,35], the spatial distribution of these two key oceanographic variables were analysed at the same coastal locations as the satellite shoreline analysis. This was undertaken using ECMWF global products, the ERA5 wave reanalysis and daily sea-level anomalies from satellite altimetry (detrended to reduce sea-level rise, see Methods). Figure 2 shows regional differences in wave energy flux during positive and negative ENSO phases, considering both boreal winter and all seasons. The impact of ENSO on sea-level anomalies across Pacific regions is indicated in Figure 3.

The widespread regional erosion during El Niño phases observed particularly in the Eastern Pacific is consistent with a concurrent increase in wave energy flux in USA and Mexico (22% and 14% increase during boreal winter, respectively) and significant increases (+5-10 cm) in sea-level anomalies along the whole Eastern boundary. In Peru and Chile, wave energy flux shows a mixed response to El Niño, suggesting elevated sea levels may control the observed erosion response in these regions during El Niño phases. This likely accounts for the lesser widespread shoreline erosion observed in Peru and Chile (47% and 33% of all transects, all seasons) compared to USA and Mexico (54% and 63%, boreal winter). During La Niña phases, deviations in both wave energy flux and sea-level anomalies generally indicate an inverse response in the Eastern Pacific, consistent with the observed overall shoreline accretion during this phase.

In the Western Pacific, sea-level anomalies are relatively weak and for the most part not-statistically significant. However, the strong and out-of-phase coastal response to ENSO observed in south-east Australia (Figs. 1c and 1d) is also associated with an increase in wave energy flux (+5%) during La Niña phases and decrease (-5%) during El Niño phases as reported in Figs. 2c and 2d (all seasons). The mixed shoreline response observed along the island nations is likely the result of their widely diverse coastline orientation (Supplementary Fig. 2) and subsequent exposure to a multitude of wave sources across the Pacific (e.g., New Zealand and Hawaii being exposed to both Northern and Southern Pacific wave climates). This sensitivity to localized wave exposure and associated coastal response is also evident in several sub-regions (e.g., Baja California, northern Peru).

Extreme beach erosion and links to major ENSO events

In addition to regional patterns in coastal erosion and accretion due to ENSO (Fig. 1), shoreline time-series were analysed to identify extreme beach erosion associated with major ENSO events of the past 35 years. Extreme beach erosion was defined by the lowest 5% of seasonally-averaged shorelines and collated for each region to highlight widespread extreme erosion in either El Niño, La Niña or Neutral years (Methods). This temporal variability in extreme beach erosion is shown for each region in Figure 4.

Overall, the regional pattern is consistent with the more general shoreline erosion and accretion patterns in Figure 1, with extreme beach erosion associated with major El Niño events in the Eastern Pacific and, inversely, major and prolonged La Niña phases in south-east Australia. In the Eastern Pacific, this analysis reveals that the 1997/1998 event was the most erosive over the past 35 years, during which close to 50% of all transects experienced widespread extreme erosion across the four regions from USA to Chile (Figs. 4e-h). The 2009/2010 and 2015/2016 El Niño events also indicate extreme regional erosion in USA and Mexico, but to a lesser spatial extent (i.e., 29% compared to 42% in USA, and 22% compared to 57% in Mexico for the 2009/2010 and 1997/1998 events, respectively) and are not evident in Peru and Chile.

Also apparent in Figure 4 are examples of extreme coastal erosion in successive years following major ENSO events. For example, in the Eastern Pacific the 1997/1998 El Niño is followed by a La Niña year, but the percentage of extremely eroded transects in 1998/1999 remains high as beaches may still be in a slow recovery period (similarly in Australia, 2012/2013 does not correspond to a major La Niña phase but follows two consecutive years of strong La Niña conditions). Along the complex coastlines of the three smaller island nations, no years in particular stand out in terms of widespread extreme erosion.

Regional variability in ENSO and future Pacific coastal response

We have shown how the El Niño/Southern Oscillation causes large regional variability in coastal erosion and accretion in the Pacific Basin. Interannual shoreline response to ENSO is most coherent along the Eastern Pacific and south-east Australia, but out-of-phase. In view of current ENSO projections, which point towards an increase in the frequency of extreme El Niño events[3,36] and a shift in their 'flavor'[37] from Eastern Pacific (EP) to Central Pacific (CP)[38,39], our analyses suggest that the Eastern Pacific in particular emerges as the sector of the Pacific most susceptible to enhanced coastal erosion and interannual shoreline variability in a warming climate.

Furthermore, the temporal variability in extreme coastal erosion spanning the past 35 years suggest that, along the Eastern Pacific, recent El Niño events with a strong CP component[40–43] (i.e. the 2003/2004, 2009/2010 and 2015/2016 events) have resulted in less widespread erosion compared to the canonical 1997/1998 EP event. This is consistent with the observed oceanographic forcing which shows that during the three largest events in the study period, the largest increase in wave energy flux and sea-level anomalies occurred during the 1997/1998 event, with relatively weaker anomalies during the 2015/2016 mixed event and substantially weaker anomalies during the 2009/2010 CP event (Supplementary Fig. 7).

Future research should focus on understanding the mechanisms by which different types of El Niño influence oceanographic forcing across the oceanic basin and how these may affect sandy coastlines in a CP-El Niño dominated climate.

References

1. Luijendijk, A. *et al.* The State of the World's Beaches. *Sci. Rep.* 1–11 (2018). doi:10.1038/s41598-018-24630-6

2. Nyberg, B. & Howell, J. A. Global distribution of modern shallow marine shorelines. Implications for exploration and reservoir analogue studies. *Mar. Pet. Geol.* **71**, 83–104 (2016).

3. Cai, W. *et al.* Increasing frequency of extreme El Niño events due to greenhouse warming. *Nat. Clim. Chang.* **4**, 111–116 (2014).

4. Woollings, T. & Blackburn, M. The north Atlantic jet stream under climate change and its relation to the NAO and EA patterns. *J. Clim.* **25**, 886–902 (2012).

5. Reguero, B. G., Losada, I. J. & Méndez, F. J. A recent increase in global wave power as a consequence of oceanic warming. *Nat. Commun.* **10**, 1–14 (2019).

6. Mentaschi, L., Vousdoukas, M. I., Voukouvalas, E., Dosio, A. & Feyen, L. Global changes of extreme coastal wave energy fluxes triggered by intensified teleconnection patterns. *Geophys. Res. Lett.* **44**, 2416–2426 (2017).

7. Theuerkauf, E. J., Rodriguez, A. B., Fegley, S. R. & Luettich, R. A. Sea level anomalies exacerbate beach erosion. *Geophys. Res. Lett.* **41**, 5139–5147 (2014).

8. Ranasinghe, R. Assessing climate change impacts on open sandy coasts: A review. *Earth-Science Reviews* (2016). doi:10.1016/j.earscirev.2016.07.011

9. Li, N., Yamazaki, Y., Roeber, V., Cheung, K. F. & Chock, G. Probabilistic mapping of storm-induced coastal inundation for climate change adaptation. *Coast. Eng.* **133**, 126–141 (2018).

10. Troup, A. J. The 'southern oscillation'. *Q. J. R. Meteorol. Soc.* **91**, 490–506 (1965).

11. Odériz, I., Silva, R., Mortlock, T. R. & Mori, N. ENSO Impacts on Global Wave Climate and Potential Coastal Hazards. *J. Geophys. Res. Ocean.* (2020). doi:10.1029/2020jc016464

12. White, N. J. *et al.* Australian sea levels-Trends, regional variability and influencing factors. *Earth-Science Reviews* **136**, 155–174 (2014).

13. Ward, P. J., Beets, W., Bouwer, L. M., Aerts, J. C. J. H. & Renssen, H. Sensitivity of river discharge to ENSO. *Geophys. Res. Lett.* **37**, 1–6 (2010).

14. Vidal-Ruiz, J. A. & Ruiz de Alegría-Arzaburu, A. Variability of sandbar morphometrics over three seasonal cycles on a single-barred beach. *Geomorphology* **333**, 61–72 (2019).

15. Peterson, C. D., Jackson, P. L., O'Neil, D. J., Rosenfeld, C. L. & Kimerling, A. J. Littoral Cell Response to Interannual Climatic Forcing 1983-1987 on the Central Oregon Coast, USA. *J. Coast. Res.* **6**, 87–110 (1990).

16. Barnard, P. L. *et al.* The impact of the 2009-10 El Niño Modoki on U.S. West Coast beaches. *Geophys. Res. Lett.* **38**, 1–7 (2011).

17. Barnard, P. L. *et al.* Extreme oceanographic forcing and coastal response due to the 2015-2016 El Niño. *Nat. Commun.* **8**, (2017).

18. Kuriyama, Y., Banno, M. & Suzuki, T. Linkages among interannual variations of shoreline, wave and climate at Hasaki, Japan. *Geophys. Res. Lett.* **39**, 2–5 (2012).

19. Phinn, S. R. & Hastings, P. A. Southern Oscillation Influences on the Gold Coast's Summer Wave Climate. *J. Coast. Res.* **11**, 946–958 (1995).

20. Ranasinghe, R., McLoughlin, R., Short, A. & Symonds, G. The Southern Oscillation Index, wave climate, and beach rotation. *Mar. Geol.* **204**, 273–287 (2004).

21. Barnard, P. L. *et al.* Coastal vulnerability across the Pacific dominated by El Niño/Southern Oscillation. *Nat. Geosci.* **8**, 801–807 (2015).

22. Young, A. P. *et al.* Southern California Coastal Response to the 2015–2016 El Niño. *J. Geophys. Res. Earth Surf.* **123**, 3069–3083 (2018).

23. Gorelick, N. *et al.* Google Earth Engine: Planetary-scale geospatial analysis for everyone. *Remote Sens. Environ.* **202**, 18–27 (2017).

24. Pardo-Pascual, J. E., Almonacid-Caballer, J., Ruiz, L. A. & Palomar-Vázquez, J. Automatic extraction of shorelines from Landsat TM and ETM+ multi-temporal images with subpixel precision. *Remote Sens. Environ.* **123**, 1–11 (2012).

25. Hagenaars, G., de Vries, S., Luijendijk, A. P., de Boer, W. P. & Reniers, A. J. H. M. On the accuracy of automated shoreline detection derived from satellite imagery: A case study of the sand motor mega-scale nourishment. *Coast. Eng.* **133**, 113–125 (2018).

26. Vos, K., Harley, M. D., Splinter, K. D., Simmons, J. A. & Turner, I. L. Sub-annual to multi-decadal shoreline variability from publicly available satellite imagery. *Coast. Eng.* **150**, 160–174 (2019).

27. Mentaschi, L., Vousdoukas, M. I., Pekel, J.-F., Voukouvalas, E. & Feyen, L. Global long-term observations of coastal erosion and accretion. *Sci. Rep.* **8**, 12876 (2018).

28. Vos, K., Harley, M. D., Splinter, K. D., Walker, A. & Turner, I. L. Beach Slopes From Satellite-Derived Shorelines. *Geophys. Res. Lett.* **47**, (2020).

29. Vos, K., Splinter, K. D., Harley, M. D., Simmons, J. A. & Turner, I. L. CoastSat: A Google Earth Engine-enabled Python toolkit to extract shorelines from publicly available satellite imagery. *Environ. Model. Softw.* **122**, 104528 (2019).

30. Wolter, K. & Timlin, M. S. El Niño/Southern Oscillation behaviour since 1871 as diagnosed in an extended multivariate ENSO index (MEI.ext). *Int. J. Climatol.* **31**, 1074–1087 (2011).

31. Young, I. R. Seasonal variability of the global ocean wind and wave climate. *Int. J. Climatol.* **19**, 931–950 (1999).

32. Russell, P. E. Mechanisms for beach erosion during storms. *Cont. Shelf Res.* **13**, 1243–1265 (1993).

33. Masselink, G. *et al.* Extreme wave activity during 2013/2014 winter and morphological impacts along the Atlantic coast of Europe. *Geophys. Res. Lett.* 2135–2143 (2016). doi:10.1002/2015GL067492.Received

34. Phillips, M. S., Harley, M. D., Turner, I. L., Splinter, K. D. & Cox, R. J. Shoreline recovery on wave-dominated sandy coastlines: the role of sandbar morphodynamics and nearshore wave parameters. *Mar. Geol.* **385**, 146–159 (2017).

35. Davidson, M. A., Turner, I. L., Splinter, K. D. & Harley, M. D. Annual prediction of shoreline erosion and subsequent recovery. *Coast. Eng.* **130**, 14–25 (2017).

36. Wang, G. *et al.* Continued increase of extreme El Ninõ frequency long after 1.5 C warming stabilization. *Nat. Clim. Chang.* **7**, 568–572 (2017).

37. Capotondi, A. *et al.* Understanding ENSO Diversity. *Bull. Am. Meteorol. Soc.* **96**, 921–938 (2014).

38. Yeh, S. W. *et al.* El Niño in a changing climate. *Nature* **461**, 511–514 (2009).

39. Freund, M. B. *et al.* Higher frequency of Central Pacific El Niño events in recent decades relative to past centuries. *Nat. Geosci.* **12**, 450–455 (2019).

40. Ashok, K., Behera, S. K., Rao, S. A., Weng, H. & Yamagata, T. El Niño Modoki and its possible teleconnection. *J. Geophys. Res. Ocean.* **112**, (2007).

41. Kao, H. Y. & Yu, J. Y. Contrasting Eastern-Pacific and Central-Pacific types of ENSO. *J. Clim.* **22**, 615–632 (2009).

42. Santoso, A., Mcphaden, M. J. & Cai, W. The Defining Characteristics of ENSO Extremes and the Strong 2015/2016 El Niño. *Reviews of Geophysics* **55**, 1079–1129 (2017).

43. Paek, H., Yu, J. Y. & Qian, C. Why were the 2015/2016 and 1997/1998 extreme El Niños different? *Geophys. Res. Lett.* **44**, 1848–1856 (2017).

44. Masselink, G. & Short, A. D. The effect of tide range on beach morphodynamics and morphology: a conceptual beach model. *J. Coast. Res.* **9**, 785–800 (1993).

45. Hersbach, H. *et al.* The ERA5 global reanalysis. *Q. J. R. Meteorol. Soc.* **146**, 1999–2049 (2020).

46. Carrere, L., Lyard, F., Cancet, M., Guillot, A. & Picot, N. FES 2014, a new tidal model—Validation results and perspectives for improvements. in *Proceedings of the ESA living planet symposium* 9–13 (2016). doi:https://www.aviso.altimetry.fr/

47. OSM. OpenStreetMap contributers: Planet dump retrieved from https://planet.osm.org. (2017).

48. Castelle, B. *et al.* Satellite-derived shoreline detection at a high-energy meso-macrotidal beach. *Geomorphology* 107707 (2021). doi:10.1016/j.geomorph.2021.107707

49. Izumo, T. *et al.* Influence of the state of the Indian Ocean Dipole on the following years El Nĩo. *Nat. Geosci.* **3**, 168–172 (2010).

Declarations

Data Availability

The full satellite-derived shoreline dataset generated and analysed in the current study is available in the following Zenodo data repository: https://doi.org/10.5281/zenodo.5035998.

Acknowledgements

The authors would like to thank the United States Geological Survey / NASA for providing high-quality open-access data to the scientific community, Google Earth Engine for facilitating the access to the archive of publicly available satellite imagery, NOAA for maintaining updated time-series of the major climate indices, ECMWF for the reanalysis ERA5 data and multi-mission altimetry dataset, CNES / LEGOS / CLS / AVISO for producing the global tide model FES2014 and Frederic Briol for developing the Python wrapper and the OpenStreetMap project and contributors (https://www.openstreetmap.org) for their extensive geospatial database. The lead author is supported by a UNSW Scientia PhD scholarship.

Author Contributions

K.V., M.H.D., I.L.T. and K.D.S. devised the study, designed the figures and wrote the manuscript. K.V. processed the data (shorelines, waves and sea level anomalies) and performed the analysis. All authors discussed the results and reviewed the manuscript.

Methods

Sandy beaches dataset. A first pass to identify suitable sandy beaches in the Pacific Basin to investigate regional variability controlled by ENSO was undertaken based on two primary criteria: (1) only wave-dominated sandy coastlines (i.e., coastlines primarily controlled by wave, rather than tidal, processes); and (2) the availability of Landsat images for satellite-derived shoreline mapping. Wave-dominated coastlines were classified based on the Relative Tidal Range (RTR)[44], calculated here as the ratio between the average deep-water Significant Wave Height, obtained from ERA5 reanalysis[45] and the Spring Tidal Range, obtained from the FES2014 global tide model[46]. Supplementary Figure 1 depicts the spatial distribution of Significant Wave Height (subplot a), Spring Tidal Range (subplot b) and the resulting RTR (subplot c). Coastlines with an RTR < 3 were classified as wave-dominated, while the other coastlines were labelled as tide-modified (RTR = 3-10) or tide-dominated (RTR = 10-50). Regions excluded of this study based on this criterion included north-east Australia, China, Alaska, Canada and Central America.

Regarding image availability, Landsat images suitable for time-series analysis are categorized as Tier 1 due to their consistent quality through time and across instruments. The availability of Tier 1 Landsat images between 1984 and 2020 (Landsat 5, 7, 8) varies across the Pacific Basin, as shown in Supplementary Figure 1d. For example, islands in the south-west Pacific (including Papua New Guinea and the Philippines) and in the Artic, as well as the shores of Central America, do not contain sufficient images (minimum set at 600) to achieve continuous monitoring over the 35-year study period. Therefore, these regions were also discarded from the analysis. Based on the two criteria described above, a total of 7 regions were identified: south-east Australia, New Zealand, Chile, Peru, Mexico's west coast, USA's west coast and Japan. For each region, a dataset of sandy beach locations was compiled using the OpenStreetMap database[47] and manually digitized where necessary. The sandy shoreline locations were then used to generate 100 m alongshore-spaced shore-normal transects.

From a first-pass dataset of more than 100,000 beach transects using the two criteria above, a secondary, more-detailed, filtering step was applied based on the following conditions:

- Transects where shoreline time-series (see next section on shoreline mapping) contained insufficient data for beach slope estimation (and hence tidal correction). This corresponded to a defined lower limit of 180 shorelines at each transect, or 5 shorelines/year [75% of the total filtered transects in this second pass]
- Transects where the shoreline time-series indicated a strong linear trend of erosion or accretion (threshold ±3m/year based on [1]), that are likely evidence of non-ENSO influences on the shoreline (e.g. major beach nourishments, tectonic shifts, land subsidence) [10% of filtered transects]
- Transects along small pocket beaches (less than 500 m in length) that may be dominated by cellular beach circulation effects [5% of filtered transects]
- Transects along high-energy meso-macrotidal beaches (but still classified as wave-dominated) as these require a more sophisticated water level correction for accurate shoreline mapping[48]. These include sandy beaches along the Oregon and Washington coasts as well as localised stretches of coastline along New Zealand's West coast [10% of filtered transects]

This amounted to a final dataset of 72,000 beach transects across the 7 regions. Supplementary Figure 2 illustrates the spatial extent of this dataset, including the number of transects and their orientation for each region.

Satellite-derived shorelines. The CoastSat open-source Python toolkit[29] (available at https://github.com/kvos/CoastSat) was used to download Landsat images between 1984 and 2020 at each beach (using the Google Earth Engine API[23]) and automatically map the position of the shoreline on each image. Briefly, CoastSat's detection algorithm combines a supervised image classification and a sub-pixel resolution border segmentation to map the position the instantaneous boundary between sand and water with a shoreline accuracy of 10-15 m[26]. A noteworthy improvement over the default CoastSat toolbox was to create a more generalised classifier (originally trained on 5 Australian beaches) using tens of images from sites across the 7 regions, including Chilean black sand beaches, bright sand Atacama Desert beaches, Mexican tropical beaches as well as Japanese Artic beaches. Thus, this extended classifier was capable of identifying sandy pixels at a wide range of coastal environments, making the shoreline detection more robust at the Pacific-basin scale. The intersection of the two-dimensional shorelines with the shore-normal transects were subsequently calculated to produce time-series of cross-shore shoreline change at each transect.

Tidal correction. Since every satellite image was taken at a different stage of the tide, the time-series of shoreline change obtained in the previous step were tidally-corrected to remove high-frequency shoreline changes related to tidal variations. To do this, water levels at the time of image acquisition and an estimate of the beach slope are necessary. Since obtaining measured water levels for each beach at the basin scale is not plausible, modelled tides from the FES2014 global tide model[46] were used. The beach slope along each transect was then estimated from the satellite-derived shorelines and corresponding tide levels using a method described in [28] (available at https://github.com/kvos/CoastSat.slope). This technique applies a frequency domain analysis to the shoreline time-series to find the optimum slope that, when used for tidal correction, minimises high-frequency tidal fluctuations relative to lower-frequency erosion/accretion signals.

Anomalies in shoreline position during ENSO phases. To evaluate the effect of ENSO on shoreline changes, the seasonally-averaged shoreline positions during El Niño and La Niña phases were compared to the long-term average with a distribution-free statistical test (Fig. 1). Two separate anomaly analyses were performed, one including shorelines from all four seasons and one using only the boreal winter (DJF) averages to address the strong seasonality in shoreline variability of the northern hemisphere[31]. El Niño and La Niña phases were defined by the periods of time during which the intensity of the Multivariate ENSO Index[30] (MEI) was larger than half of its standard deviation (similar to [42]). Supplementary Figures 3 and 4 show examples of detrended time-series of shoreline change along two different transects located respectively along Ocean Beach (San Francisco, USA) and Narrabeen (Sydney, Australia). The MEI time-series and the observed anomalies in shoreline position are also illustrated in the figures. These two examples show that at a seasonal northern hemisphere beach like Ocean Beach

(Supplementary Fig. 3), the ENSO anomalies are more pronounced during the boreal winter (DJF), while at a southern hemisphere beach with no apparent seasonality like Narrabeen (Supplementary Fig. 4), the anomalies are evident during all four seasons.

To test if the observed anomalies are statistically different than the long-term average, the shoreline positions during each ENSO period were compared to the long-term average with a Wilcoxon signed-rank test — the distribution-free equivalent of a one-sample t-test. The resulting p-value indicate the probability of the mean of the population being greater or less than (one-tailed) the long-term average. The statistical test was repeated for both ENSO phases and evaluated for the boreal winter (DJF) anomalies as well as anomalies from all four seasons, generating four p-values for each transect, as presented in the four subplots of Figure 1 in the main manuscript.

Anomalies in wave energy flux during ENSO phases. A similar analysis was performed to quantify the effect of ENSO on wave energy flux around the Pacific (Fig. 2). Six-hourly time-series of significant wave height and mean wave period from the 50 km-resolution ECMWF ERA5 reanalysis[45] were used to calculate wave energy flux in watts per metre of wave front:

$$P = \frac{\rho g^2 {H_s}^2 T}{64\pi}$$

where kg/m^3, g is the gravitational constant, significant wave height and mean wave period. An example of wave energy flux time-series at the closest grid point to Ocean Beach (San Francisco, USA) is shown in Supplementary Figure 5. The statistical significance of the observed deviations from the long-term average wave energy flux during both ENSO phases was also quantified with a Wilcoxon signed-rank test as described above.

Sea-level anomalies during ENSO phases. Time-series of daily sea-level anomalies based on satellite altimetry provided by ECMWF and Copernicus Climate Change Service between 1993 and 2020 were used to investigate corresponding sea level anomalies during ENSO phases. Sea-level anomaly time-series were detrended to reduce any sea-level rise signal and the differences between El Niño and La Niña phases were computed on the subsequent seasonally-averaged time-series. An example of sea-level anomaly time-series at the closest grid point to Ocean Beach (San Francisco, USA) is illustrated in Supplementary Figure 6. As per above, the statistical significance of the observed differences in sea level anomalies was also evaluated with a Wilcoxon signed-rank test.

Regional extreme beach erosion. Seasonally-averaged time-series of shoreline variability along each transect were first divided into yearly bins, defined from 1 August to 31 July. For each yearly bin, the most eroded datapoint was selected and compared to the lowest 1% and 5% shoreline positions in the record (Fig. 4). To classify El Niño, La Niña or Neutral years, the same approach as in [49] was used and selected the years when the Oct-Nov-Dec (OND) average of the MEI was above (for El Niño years) or below (for La Niña years) half of its standard deviation.

Figures

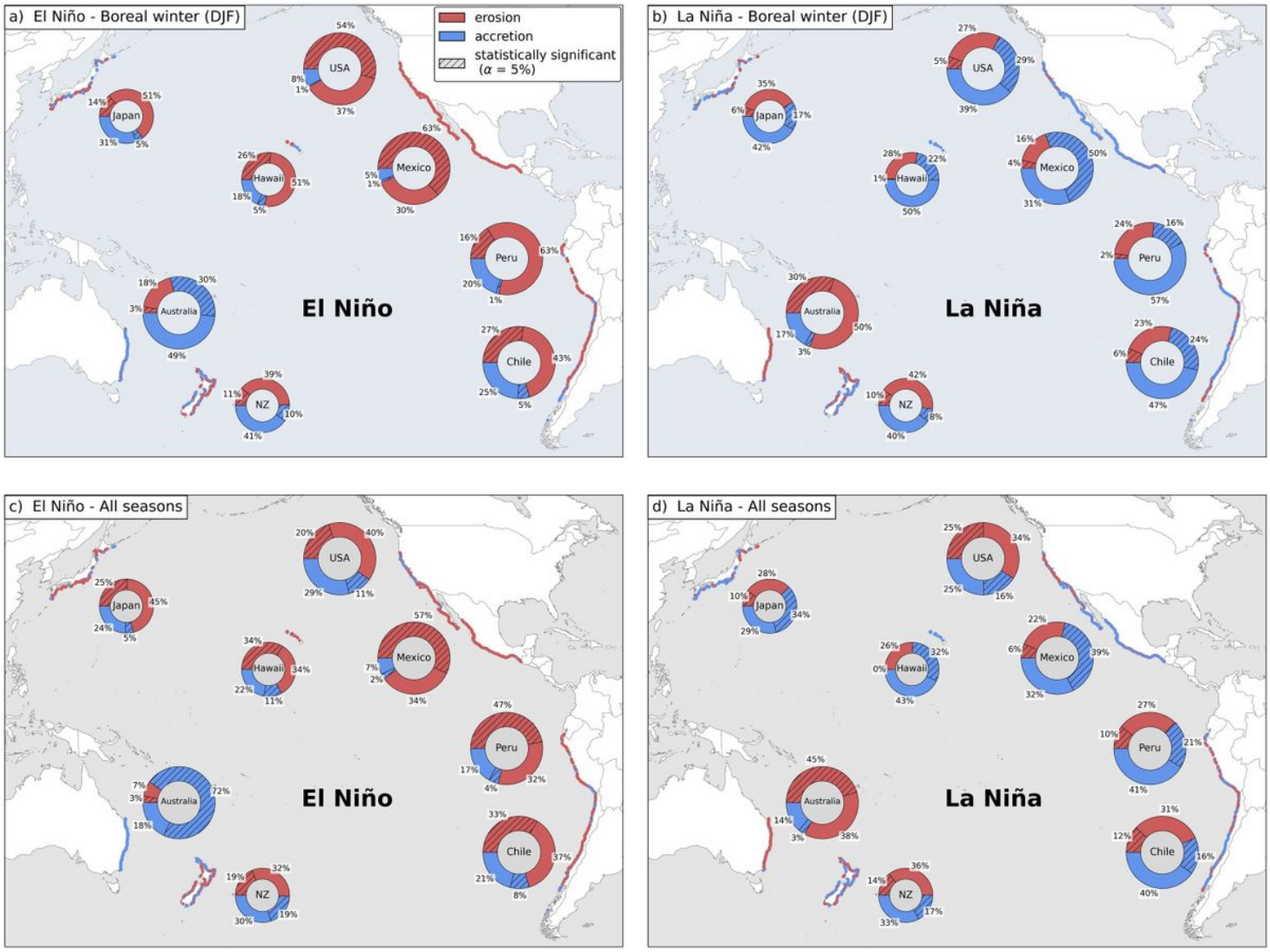

Figure 1

Regional patterns of shoreline response to ENSO in the Pacific. Teleconnections between shoreline variability and ENSO along wave-dominated sandy beaches in the Pacific during the boreal winter season only (a,b) and during all four seasons (c,d). The pie charts indicate the proportion of transects that experience enhanced erosion (red) or accretion (blue) during El Niño (a,c) and La Niña (b,d) phases for each region. The proportion of transects along which the anomalies are statistically significant at a 95% confidence level (Methods) are hashed.

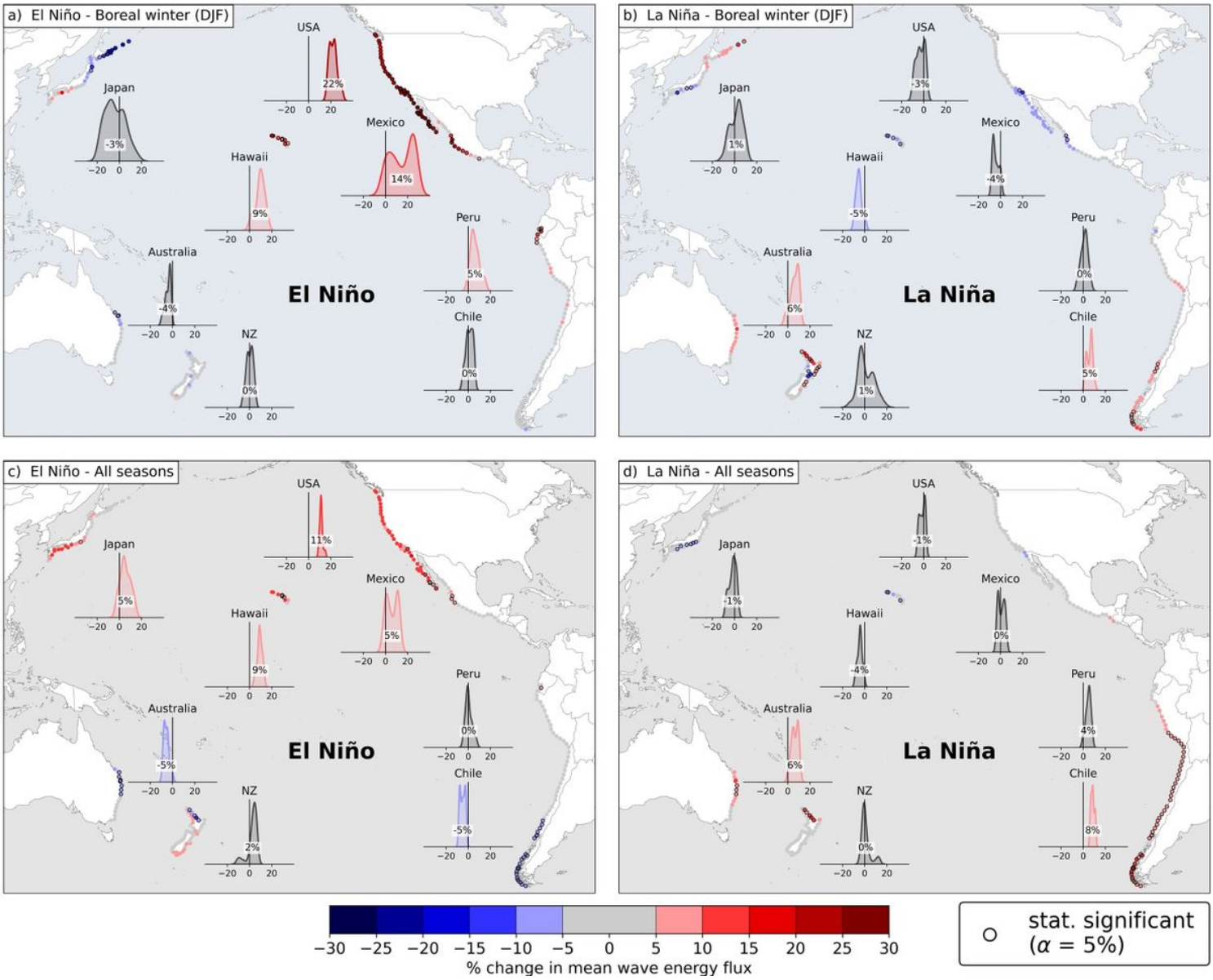

Figure 2

Teleconnections between wave energy flux and ENSO phases in the Pacific. The maps show the percentage change in mean wave energy flux during the boreal winter season only (a,b) and during all four seasons (c,d) for El Niño (a,c) and La Niña (b,d) phases. Anomalies are calculated along a 50 km-grid using ERA5 wave data between 1979-2020 (Methods). The anomalies that are statistically significant at a 95% confidence interval are circled. A probability distribution function (PDF) of all the grid points belonging to each region is plotted as well, the colour of the distribution represents the position of the mean along the colour bar (e.g., grey if the mean of the distribution is between -5 and 5% anomaly).

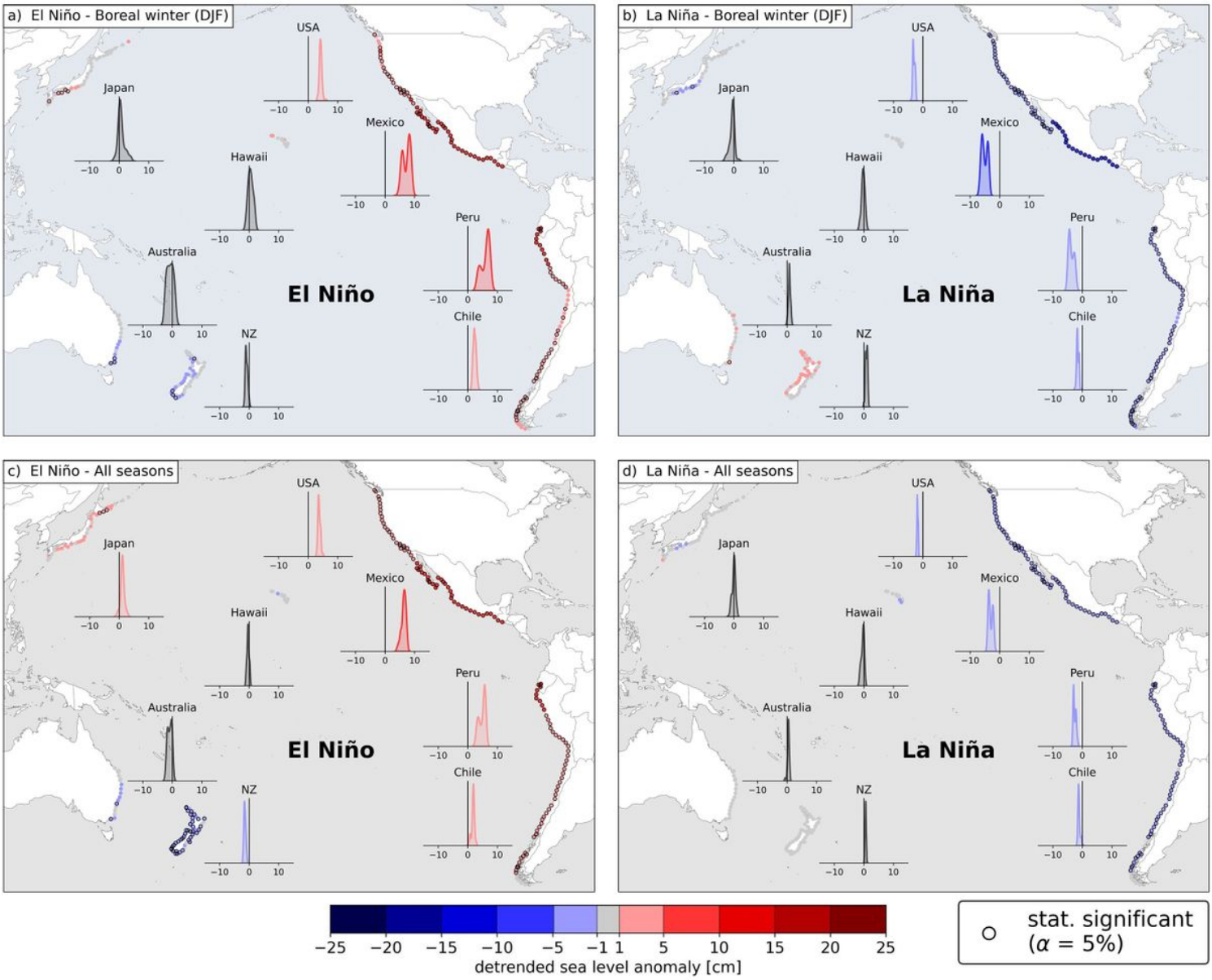

Figure 3

Teleconnections between sea-level anomalies and ENSO phases in the Pacific. The maps show differences in detrended sea-level anomalies during the boreal winter season only (a,b) and during all four seasons (c,d) for El Niño (a,c) and La Niña (b,d) phases calculated along a 50 km-grid using the ECMWF multi-mission altimetry dataset between 1993-2020 (Methods). The anomalies that are statistically significant at a 95% confidence interval are circled. A probability distribution function (PDF) of all the grid points belonging to each region is plotted as well, the colour of the distribution represents the position of the mean along the colour bar (e.g., grey if the mean is between -1 and 1 cm anomaly).

Figure 4

Extreme regional erosion over the last 35 years showing the impact of major La Niña events (1988/1989, 1999-2001, 2008-2009, 2011-2014) along the south-eastern Australian coast and major El Niño events (1997/1998, 2009/2010, 2015/2016) along the Eastern Pacific. The bar plots show the percentage of transects in each region where the seasonally-averaged shorelines were in the lowest 1% (dark gray) and 1 to 5% (light gray) for each given year in the shoreline record. El Niño years are shown in red and La Niña years in blue, while Neutral years remain gray. Subplot i) shows time-series of the monthly Multivariate ENSO Index (MEI), with Oct-Nov-Dec (OND) averages used to identify El Niño, La Niña and Neutral years based on a 0.5 standard deviation threshold (Methods).

Supplementary Files

This is a list of supplementary files associated with this preprint. Click to download.

- supplementaryinformationVosetal.docx